Tailored porosity in additive manufacturing of 7075 aluminum alloy for crack suppression and high strength

Abstract: Laser-directed energy deposition (LDED) additive manufacturing of 7075 aluminum (Al) alloy is highly challenging due to the inherent poor printability and high cracking tendency. Here, we disclose a new approach to suppress cracking in LDED 7075 Al alloy by engineered porosity (about 1.14%). The crack-free 7075 Al alloy was achieved by slightly sacrificing the densification. Further increasing the density of the material by increasing laser energy input leads to cracking in the material. The mechanisms of minor pores in alleviating cracks mainly in three aspects: (i) Pores disrupt the epitaxial growth of columnar grains; (ii) free-form surfaces surrounding pores could release the accumulated residual stress, and (iii) more dislocations near pore drive nucleation of near equiaxed grains. The LDED-processed crack-free 7075 Al alloy after heat treatment shows an ultimate tensile strength of 464 ± 12 MPa and break elongation of 9.7 ± 1.2%, attaining a good strength-ductility synergy among many additively manufactured 7075 Al alloys in the current literature. Unlike the mainstream additive manufacturing of metallic materials, which pursues high densification to attain high-performance components, this work demonstrates the positive roles of pores in the additive manufacturing of cracking-sensitive materials. The findings of this work highlight new insights regarding the balance between pores and cracks for better manufacturability and higher mechanical performance of materials.

Keywords: Laser-directed energy deposition; 7075 aluminium alloy; Crack suppression; Columnar grain; Printability.

1. Introduction

The 7075 Al alloys with high specific strength, good fracture toughness, and fatigue performance have been used in automotive, marine, and aerospace fields, where both high performance and intricate geometries are essential [1, 2]. Laser-directed energy deposition (LDED) stands out as a frontier additive manufacturing technology, which catches significant R&D efforts from researchers owing to its substantial benefits in manufacturing large-scale components, repairing high-value parts, and enabling multi-material configurations at high deposition rates [3, 4].

LDED of high-strength Al alloys (e.g., 7075 Al alloy) are highly challenging due to the materials' poor printability. Specifically, the solidification temperature interval of 7075 Al alloys is relatively wide (approximately 175 ˚C [5]) compared with other printable Al alloys like AlSi10Mg (solidification interval 31 ˚C [5]), resulting in heightened susceptibility to cracks in the as-builts. Additionally, the pores are also the common defects in LDED of 7075 Al alloys [6], due to the high laser reflectivity of Al powder and lack-of-fusion [7], requiring high laser energy input during LDED [8]. However, a higher energy input causes intensive elemental evaporations and oxidations [9] and also escalates thermal gradients and propensity for cracking [10]. Thus, the process window for LDED of 7075 Al alloy is severely constrained.

Cracking suppression is intractable in laser printing of 7075 Al alloy. Compared with pores, cracks are more likely to expand under applied loads and lead to more severe stress concentration, which dramatically damages the mechanical properties [11]. In recent years, considerable efforts have been dedicated to eliminating cracks in LDED 7075 Al alloys. These efforts include incorporating anti-thermal cracking alloy elements (e.g., Si, Sc, and Zr), adding reinforcement particles, and optimising deposition strategies (e.g., preheating substrate and alternating scan strategies), etc [12]. In general, the ultimate tensile strength (UTS) and yield strength (YS) of LDED-processed 7075 Al alloys after heat treatment typically fall below 400 and 300 MPa, respectively [13].

It is generally considered that pores have an adverse effect on the strength of materials via acceleration of crack initiation and propagation during deformation [14]. Hence, the mainstream additive manufacturing of metallic materials pursues high densification to attain high-performance components. Wang et al. found that high porosity will change the local thermal conductivity of the component and affect heat conduction and cooling rate, causing uneven grain structures and increasing thermal cracking sensitivity [15]. Tao et al. found that pores may cause local instability and increase the crack propagation rate [16]. However, there is a growing recognition that pores in LDED 7075 Al alloy are extremely difficult to completely eliminate due to the extremely narrow process window. In this case, leveraging pores and excavating the balanced relationship between pores and cracks to weaken the cracking susceptibility in LDED 7075 Al alloy will greatly promote the development and application of LDED-processed high-strength Al alloys.

Hence, this work investigates how the deliberately engineered pores affect cracking behaviour in LDED 7075 Al alloy, demonstrating the positive roles of pores in the additive manufacturing of cracking-sensitive materials. The findings of this work shed light on the relationship between pores and cracks in LDED of highly crack-sensitive alloys, offering fresh insights into crack mitigation strategies in additive manufacturing.

2. Materials and methods

Zinc (Zn) and magnesium (Mg) losses are common during laser processing of Al alloy, and Zn loss is more evident than Mg [17]. Hence, a high Zn content 7075 Al ingot with the composition of Al-6.60Zn-3.15Mg-1.60Cu (wt%) was customised for powder processing in this work The powder compositions measured by inductively coupled plasma optical emission spectroscopy (ICP-OES, Agilent ICPOES730) are Al-6.39Zn-2.81Mg-1.44Cu, wt%. The gas-atomised 7075 Al powder from the ingot was used as the raw materials for LDED (Fig. 1a). The cross-sections of powder particles exhibit cellular morphology without internal pores (Fig. 1b). Fig. 1c and d display the element mapping result of 7075 Al powder. The spherical 7075 Al powder particle size distribution is plotted in Fig. 1e, showing D_{10}, D_{50}, and D_{90} values of 11.4, 20.4, and 33.7 µm, respectively. The powder laser reflectivity results are shown in Fig. 1f, which suggests a higher laser reflectivity rate of about 45%.

The 7075 Al samples were printed by a Trumpf Trulaser Cell 7040 LDED system. To explore the suitable process window and understand the interplay of process parameters, porosity and cracks, different laser powers (i.e., 1050 W, 1300 W, 1600 W and 1900 W) were applied, with the laser scan speed, powder feeding rate, and hatch spacing fixed at 1500 mm/min, 1.0 g/min, and 50 % overlap rate, respectively. The samples deposited with 1900, 1600, 1300 and 1050 W are terms as HE, ME, NE, and LE, respectively. The layer thicknesses for the LE, ME, NE, and HE samples are about 0.125, 0.175, 0.20, and 0.225 mm, respectively. During LDED, argon gas was used as shielding and carrier gas to avoid oxidation. The carrier and shielding gas flow rates are 4 and 10 L/min, respectively. A raster scan pattern with a 90°

rotation between layers was adopted for all the samples. The volumetric energy density (E_v) was calculated according to the equation E_v= laser power / (scan speed × hatch spacing × layer thickness) [18]. Fig. 1g shows the as-built blocks (50×80×8 mm^3) with good surface quality. The heat treatment processes were solid solution at 470 ˚C for 1 hour (water quenching) followed by artificial aging at 110 ˚C (thermal couple measured sample temperature) for 18 hours (air cool). The powder laser reflectivity was tested using diffuse reflectance spectroscopy (DRS, Lambda 1050 UV-Vis-NIR Spectrophotometer) in the 400-1500 nm wavelength range with a step size of 1 nm. The powder size was measured using a Microtrac S3500 (USA) laser particle size analyser. The powder morphology and heat-treated grain morphology were observed by the scanning electron microscope (SEM, JEOL 7800) equipped with electron backscatter diffraction (EBSD, FEI 600i). The X-ray computed tomography (X-ray CT) was performed at the fein focus Yxlon X-ray CT machine with a voxel size of 0.5 µm. The microstructures of as-built 7075 Al alloy (sectioned along build direction) were characterised by an optical microscope (OM, OLYMPUS MX51), field emission transmission electron microscope (FETEM, FEI Talos F200X), and EBSD. The step size of the EBSD test was set as 0.4-1.2 µm at different magnifications. The relative density of bulk samples was estimated by ImageJ software using the OM images. The tensile test was conducted on an Instron 5982 universal testing machine equipped with an advanced video extensometer (AVE) at a loading rate of 0.5 mm/min, and three repeated tests were carried out for each condition. The detailed dimensions of the tensile specimens and their sampling locations are shown in Supplementary Materials Fig. S1.

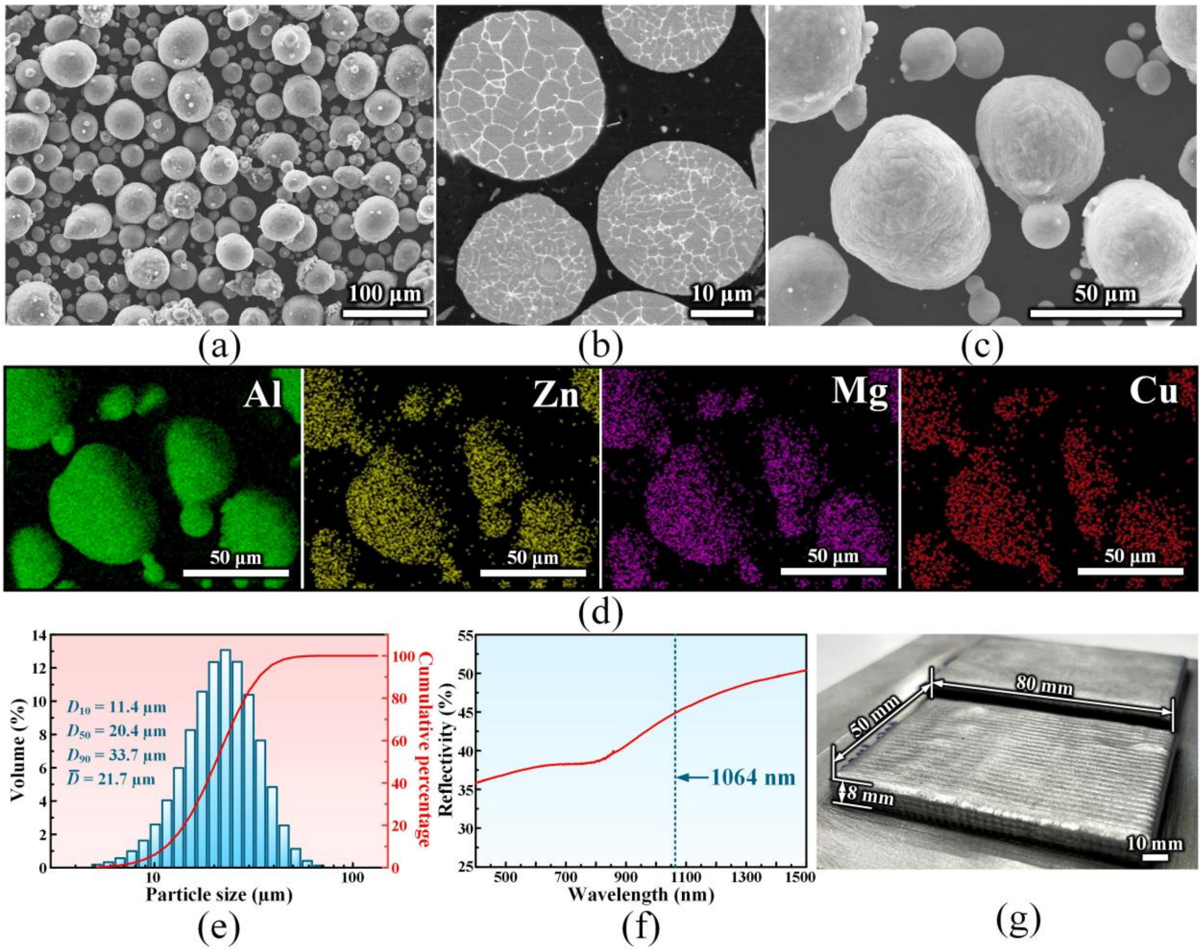

Fig. 1 Characterization of 7075 Al powders and LDED-processed 7075 Al bulk samples: (a) Morphologies of 7075 Al powder, (b) backscattered electron micrographs of the powder cross-section. (c) high-magnification SEM and (d) correlate element maps, (e) powder particle size distributions, (f) laser reflectivity of powder, and (e) LDED-processed 7075 Al bulk samples.

3. Results and discussion

3.1 Effect of process parameters on porosity and cracking

The E_v values for LE, ME, NE, and HE samples are about 350, 371, 400 and 422 J/mm^3, respectively. The different process parameters and energy inputs could affect the porosity formation and cracking susceptibility of LDED-deposited 7075 Al alloy. Fig. 2a-d shows the OM morphologies of the as-built LDED sample along the build direction. A few pores can be observed under different laser powers. The pores are mainly generated from the trapped protective gas in the melt pool and the lack of fusion due to the high laser reflectivity of powder. The relative density of the LE (1050 W) sample is about 98.86% (i.e., porosity 1.14%). With an increased laser power, both the lack-of-fusion and gas pores were significantly reduced. The fluidity and thermo-capillary convection of the melt pool were both enhanced with a higher laser powder, facilitating gas escape and a higher relative density of 99.82% (porosity 0.18%), 99.84% (porosity 0.16%), and 99.57% (porosity 0.43%) in the ME, NE and HE sample, respectively. However, the micro-cracks present in the ME, NE, and HE samples once porosity is reduced, as shown in Fig. 2b-d. The zoom-in observation on LE and HE samples along building direction by SEM are shown in Supplementary Materials Fig. S2, which clearly shows a crack-free LE sample with pores and a cracking HE sample without evident pores. This is because the higher laser power (under the same laser scan speed) could increase the thermal temperature gradient during laser deposition, which increases thermal cracking sensitivity. Moreover, note that the E_V was only increased by 6% when the laser power was increased from 1050 to 1300 W, while thermal cracking occurred thereafter, suggesting a narrow LDED process window for 7075 Al alloy. It can be speculated that the process parameters of the LE sample (1050W and 1500 mm/min) are one of the optimum parameters for LDED depositing crack-free 7075 Al alloy. Fig. 2e and f show the X-ray CT results of as-built LE and HE samples, in which microcracks parallel to the layer interface were observed in the HE sample due to hot cracking, while the LE sample remained crack-free. The CT analysis revealed that the average pore size in the LE sample was approximately 52 μm (See Fig. 2g). Upon increasing the energy input, the average pore size decreased to around 30 μm (See Fig. 2h). Notably, the pore sizes in the HE sample were significantly smaller compared to those in the LE sample. However, the CT scan of the HE samples revealed a few significantly large pores which may be generated by pore coalescence under high heat input. Furthermore, the porosity of the LE sample calculated by CT is 0.9 %, closely aligning with the image-based porosity of 1.14 %. In contrast, the defect volume fraction of the HE sample calculated from the CT scan was 1.6 %, attributable to the presence of microcracks.

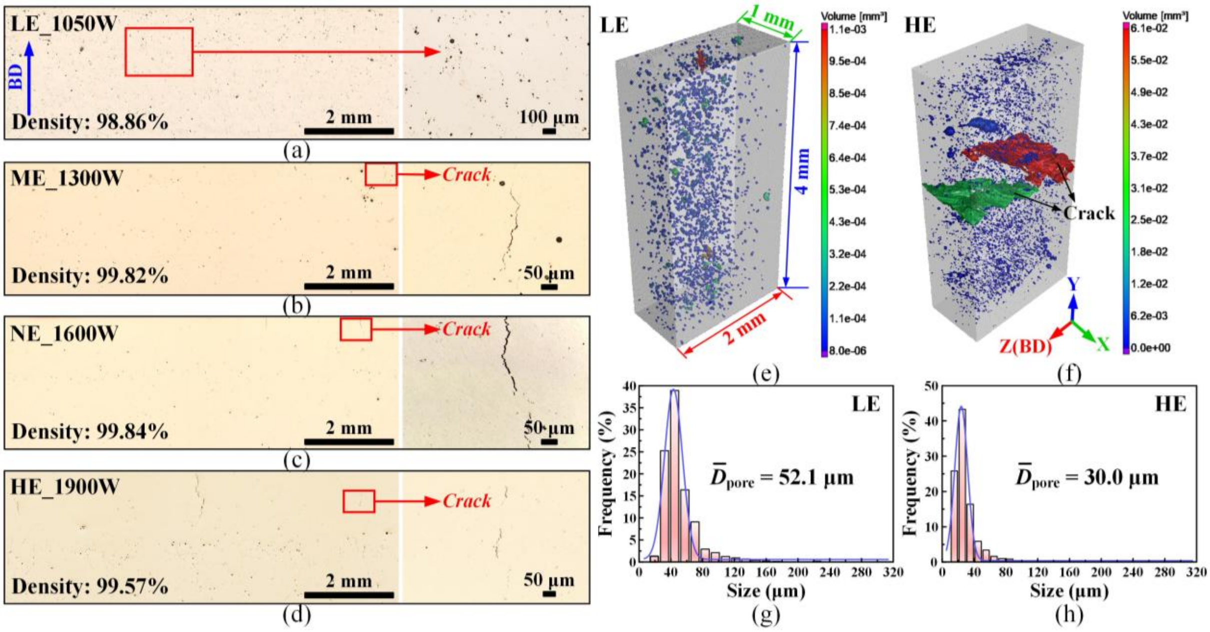

Fig. 2 Defects and relative density analysis: (a) - (d) OM images along build direction (BD) of the 1000 W (LE), 1300 W (ME), 1600 W (NE) and 1900 W (HE), samples, respectively; (e) and (f) 3D distributions of defects constructed from X-ray computed tomography (CT) results of as-built LE and HE samples, respectively; (g) and (h) pore size statistics of LE and HE samples, respectively, based on CT results.

3.2 Effect of pores on microstructure evolution

To further investigate the interaction between defects (pores and cracks) and microstructure evolution in LDED-processed Al alloy, a porosity-featured LE sample and a cracked HE sample (with excessive energy input) were selected for EBSD analysis. Fig. 3a and b display the grain morphologies of LE and HE samples, both exhibiting columnar features. The average grain sizes (in area) of LE and HE samples are about 133.9 and 356.6 μm^2, respectively, which are equivalent to equiaxed grains with average lengths of about 11.6 and 18.9 μm, respectively. Hence, the average grain size of the HE sample is larger than that of the LE sample. Fig. 3c shows the geometrically necessary dislocation (GND) map of the area near a crack in the HE sample, which corresponds to a GND value of 5.4×10^{13} m^{-2}. Fig. 3d and Fig. 3e are the GND maps of the non-porous area and porous area in the LE sample, respectively. The average GND values of non-porous areas are (8.4-8.9) ×10^{13} m^{-2}, while the average GND values of porous areas are (7.2-7.6) ×10^{13}m^{-2}, respectively. Note that the average GND value in the HE sample is the lowest, which can be attributed to the release of residual stress by crack initiation and propagation near the columnar grain. Moreover, in the LE sample, the average GND value in the porous region is lower than that in the non-porous region, suggesting that pores can relax the internal stress of the material.

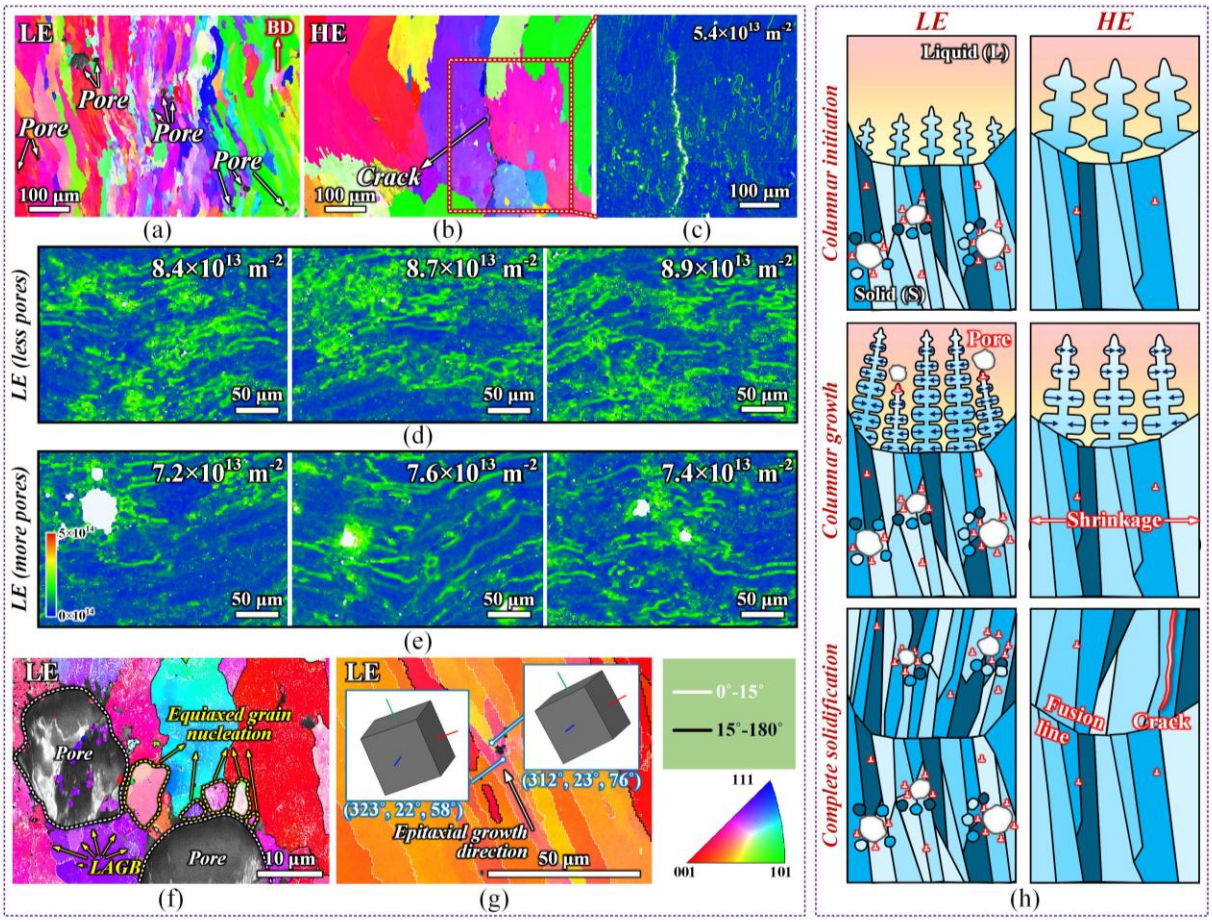

Fig. 3 EBSD analysis on LDED-processed 7075 Al alloy with low-energy (LE) and high-energy (HE): (a) and (b) inverse pole figures (IPF) of LE and HE samples, respectively; (c) geometrically necessary dislocation (GND) maps of HE sample; (d) and (e) GND maps of LE sample taken from less and rich pores regions; (f) and (g) IPF figures showing the effect of pores on grain evolutions in LE sample; and (h) Illustration of microstructure evolution mechanisms.

Additionally, some near equiaxed grains (~10 μm) are initiated near the pores in the LE sample, as depicted in Fig. 3f. The dislocation near the pore may interact and rearrange under the action of residual stress to form near-equiaxed grains with low-angle grain boundaries (LAGBs), as shown in Fig. 3f. The promoted nucleation of near-equiaxed grains also plays a crucial role in releasing residual stresses and avoiding crack initiation. Besides, as seen in Fig. 3g, the epitaxial growth of columnar grains can be disrupted when encountering a pore, and thus, the grain orientation on the other side of the pore is distinctly different from the disrupted columnar grain. Hence, it appears that the presence of pores in this 7075 Al alloy has influenced the grain morphologies and contributed to crack elimination. The underlying relationship between pores and cracks can be illustrated in Fig. 3h. First, pores can disrupt the epitaxial growth of columnar grains (Fig. 3g). Second, the stress concentration near pores is advantageous for reducing stress in the rest parts since the pores can sustain a higher stress level due to their surrounding free-form surfaces. Third, the high residual stress around pores leads to the formation of more dislocations near the solid/liquid interface, thereby increasing the nucleation rate and providing additional driving force for the nucleation of near equiaxed grains. Furthermore, recrystallization near the pores in the previously deposited layer can also promote the formation of near equiaxed grains [19]. The recrystallization driving force (E) is closely related to the dislocation density and the energy stored in LAGBs, as expressed by the following equation [20]:

$$E = \rho G b^2/2$$

where ρ, G (27.8 GPa [20]), and b (0.286 nm [20]) denote the local dislocation density near pores, shear modulus, and burgers vector, respectively. Hence, the sites around pores are more likely to induce recrystallization due to the higher dislocation density. The promoted nucleation of near-equiaxed grains also plays a crucial role in releasing residual stresses and avoiding crack initiation.

3.3 Multi-type precipitates analysis

Fig. 4 shows the precipitate distribution in the heat-treated LE sample. Note that different second-phase particles with different sizes (as indicated by arrows in Fig. 4a) are precipitated at the high-energy grain boundary. In addition, the sample exhibits prevalent dislocation networks (Fig. 4b) owing to the high cooling rate and residual stress level. The energy-dispersive X-ray spectroscopy (EDS) mapping results, shown in Fig. 4c-e, reveal that the phases precipitated at grain boundaries are $Al_{18}Cr_2Mg_3$, Al_7Cu_2Fe, $MgZn_2$ and Mg_2Si. Furthermore, high-density nano-sized η'-$MgZn_2$ phases were observed in Fig. 4f and g, with an average size of about 3.2 nm. Moreover, as shown in Fig. 4h, some Mg-rich GPI zones are fully coherent with the Al matrix along $[001]_{Al}$ without evident lattice distortion, as identified by the inverse fast Fourier transform (IFFT) in Fig. 4i.

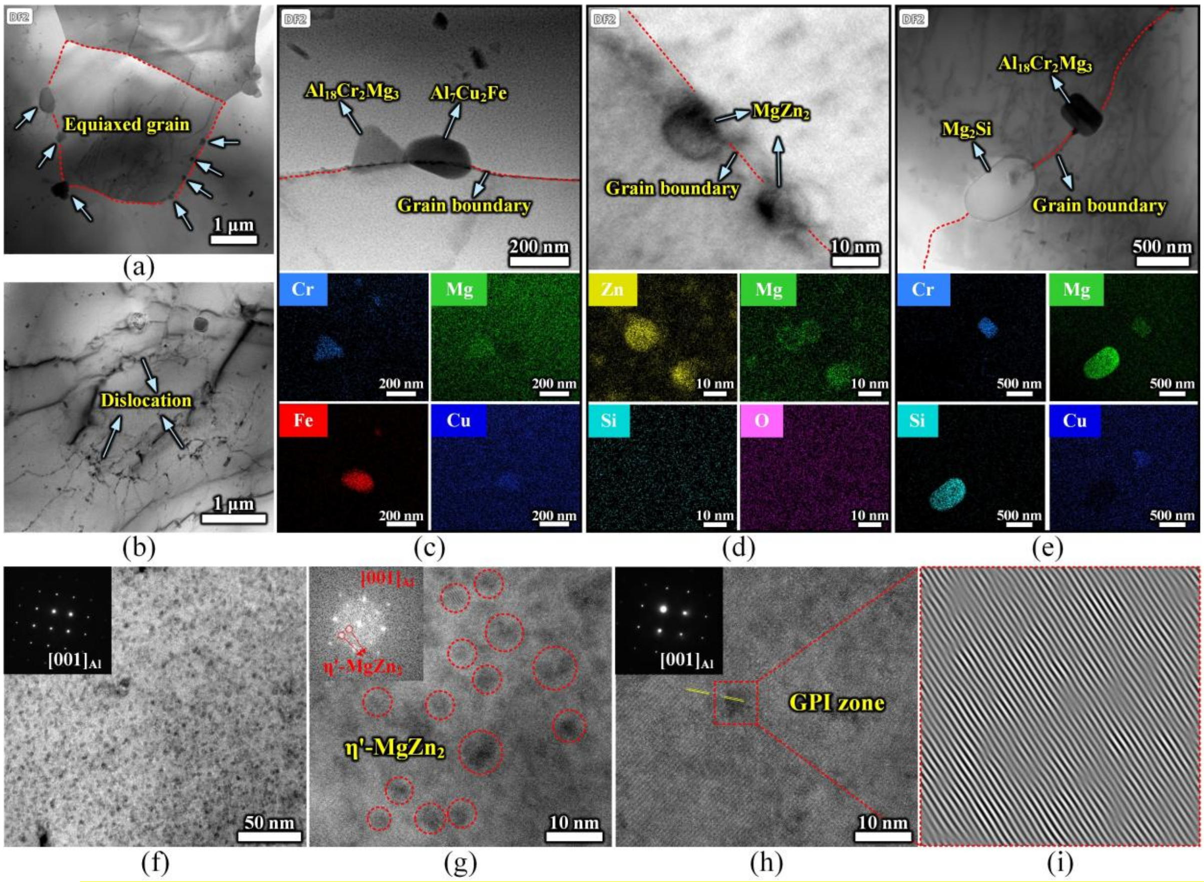

Fig. 4 TEM analysis on the heat-treated crack-free Al alloy sample processed by low-energy (LE): (a) Bright-field TEM (BF-TEM) of precipitates near grain boundaries. (b) BF-TEM of dislocations. (c-e) BF-TEM of precipitates on the grain boundaries along with corresponding EDS mapping analyses. (f) BF-TEM of nano-sized precipitates. (g) High-resolution transmission TEM (HRTEM) of η′-$MgZn_2$ phases. (h) HRTEM of GPI zone. (i) Inverse fast Fourier transform (IFFT) image of the red box in (h).

3.4 Mechanical properties and strengthening behaviour

Tensile tests were conducted to substantiate the different effects of pores and cracks on the mechanical performance. Fig. 5a exhibits the tensile stress-strain curves of heat-treated LE and HE samples. The HE sample shows a very poor mechanical property with the strength below 150 MPa and elongation below 1.0 % due to the presence of microcracks in the material (see Fig. 2b). In contrast, the LE sample, which has limited internal pores, attains significantly improved mechanical performance. The YS, UTS, and elongation of the LE samples are 356 ± 9 MPa, 464 ± 12 MPa, and 9.7 ± 1.2%, respectively, showcasing good strength-ductility synergy as compared with other LDED, laser powder bed fusion (LPBF), and casting processed 7××× (Al-Zn-Mg-Cu) Al alloys (listed in Table. S1 and highlighted in Fig. 5b and c). The reported unsatisfactory mechanical properties in the LDED- or LPBF-processed 7075 Al alloy so far could be associated with the hot cracking (especially in the LPBF process) or lack-of-fusion porosity. However, there is still a performance gap when comparing the achieved properties in our work with the ASTM standard and the state-of-the-art Al alloys printed by LPBF [21], due to the presence of about 1 vol% porosity.

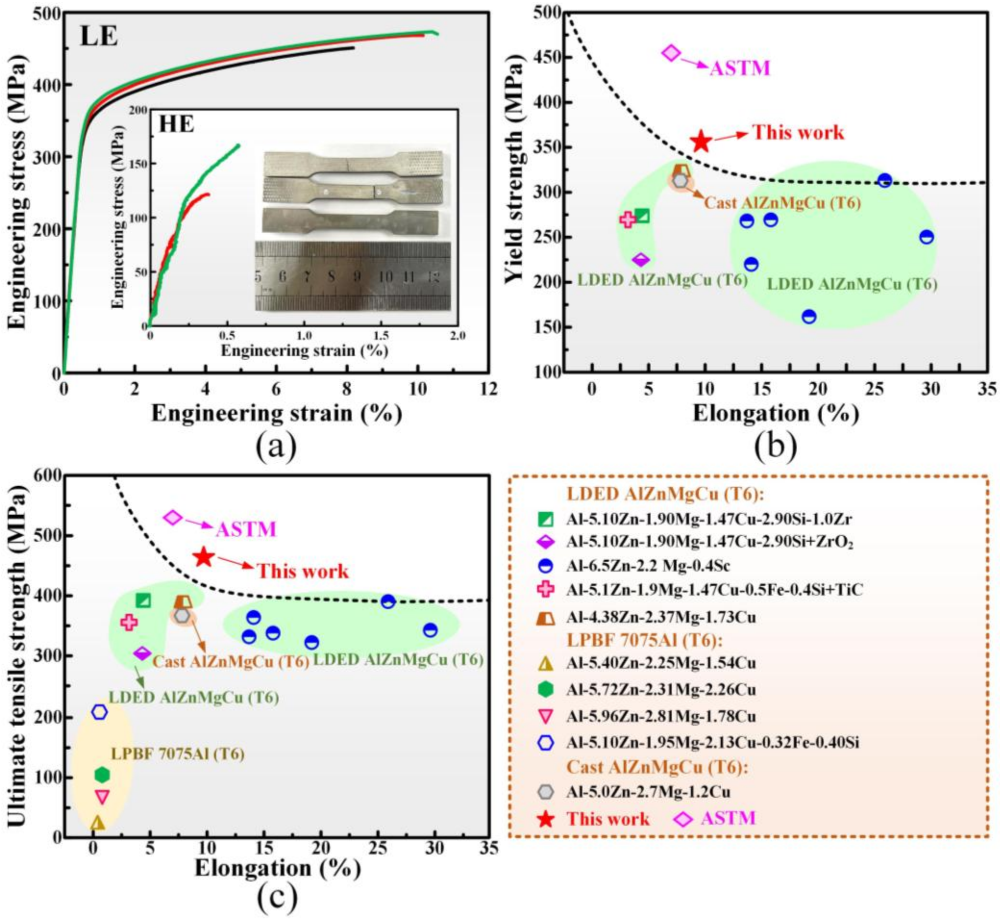

Fig. 5 Tensile properties of LDED-processed 7075 Al alloy in this work and comparison with literature: (a) Tensile engineering stress-strain curves of LDED-processed 7075 Al alloys after heat treatment. (b) yield strength (YS) versus elongation and (c) ultimate tensile strength (UTS) versus elongation of LDED-processed 7075 Al alloys in this work compared with LDED, LPBF, and casting produced 7075 Al alloys reported in the literature (all in heat-treated conditions), together with ASTM standard. The relevant pieces of literature for comparison are listed in **Supplementary Table S1**).

The achieved good strength of LDED-processed 7075 Al alloy (LE sample) after heat treatment can be attributed to the grain boundary strengthening, dislocation strengthening, precipitate strengthening, and solid solution strengthening. First, grain boundary strengthening can be estimated by [1]:

$$\sigma_{GB} = kd^{-\frac{1}{2}}$$

where $k \approx 0.14$ MPa$\cdot m^{\frac{1}{2}}$ [22] is the Hall-Petch slope. The grain size d is about 11.6 μm (Fig.

3a). Thus, the estimated contribution value from the grain boundary strengthening σ_{GB} is about 41 MPa. Second, dislocation strengthening can be expressed as [23]:

$$\sigma_d = M\alpha Gb\sqrt{\rho}$$

where $M \approx 3.06$ and $\alpha \approx 0.35$ are the Taylor factor and a constant coefficient, respectively [20]. The total dislocation population is comprised of both GNDs and statistically stored dislocations (SSDs), and the GNDs account for most of the total dislocation population in plastically deformed face-centred cubic metals (about 90% of the total dislocation population) [24]. Hence, it is estimated that $0.9\rho = \rho_{GND} = 0.83\times10^{14}$ m^{-2}, and $\rho = 0.92\times10^{14}$ m^{-2}. Thus, the σ_d is calculated as about 82 MPa. In general, precipitates with size of about 2.5 nm is considered the critical radius for the dislocation shearing in Al alloys [25]. Based on the results from HRTEM in our study, the average radius (R) of η' phases in our work is ~1.6 nm, which is below the critical radius. This indicates that the strengthening mechanism in our work is attributed to precipitation hardening (σ_p) by dislocation shearing, and follows [26]:

$$\sigma_p = M\chi(\varepsilon G)^{\frac{3}{2}}\left(\frac{Rf_V}{0.5Gb}\right)^{\frac{1}{2}}$$

where χ is a constant with a value of ~3 [26], ε represents the misfit between η' phases and Al matrix (3.08% [27]). The f_V represents the volume fraction of η' phases, approximately ~0.2 vol.% according to the Thermo-Calc prediction results (Fig. S3). Thus, the σ_p can be estimated as 206 MPa. Finally, the solid solution strengthening can be calculated by [28]:

$$\sigma_S = \Sigma_i k_i C_i$$

where k_i denotes the element strength increase efficiency (k_{Zn}=2.9 MPa/wt%, k_{Mg}= 18.6 MPa/wt%, k_{Cu}=13.8 MPa/wt% [29]), and C_i is the content of the solutes. The Thermal-Calc calculated elemental compositions after solution treatment at 470 °C are C_{Zn} =4.75, C_{Mg} =2.61, and C_{Cu} =1.47 wt% with the ICP-OES measured sample's composition as input (Fig. S4). Following the deduction of 0.2% vol.% $MgZn_2$ precipitates, the solute concentrations are determined as C_{Zn} =4.43, C_{Mg} =2.55, and C_{Cu} =1.47 wt%. This adjustment accounts for the respective densities of the $MgZn_2$ precipitates (5.34 g/cm³) and the LDED-processed alloy (2.81 g/cm³). Consequently, the σ_S is estimated as about 81 MPa, contributing to the calculated yield strength (σ_{ys}) of $\sigma_{ys} = \sigma_{GB} + \sigma_d + \sigma_p + \sigma_S$= 410 MPa. However, the measured yield strength of 356 ± 9 MPa marginally falls short of this calculation, possibly attributed to the

1.14% porosity within the material. Quantitative analysis of the strengthening mechanisms highlights precipitation hardening as the primary contributor, while acknowledging that even a minor level of porosity (about 1 % level) adversely affects the material's strength.

The good ductility of the LE sample could be associated with the porosity and the microstructures. The stress could be concentrated on the pores during tension deformation, and this multipoint stress intensification could disperse stress to delay the formation of the stress concentration band. As for the microstructure perspectives, the good ductility could be attributed to the small quantity of coherent nano-sized GPI zones and large amounts of η′ phases, as they can be cut through by dislocations during deformation to accelerate the load transfer [1].

4. Conclusion

In summary, unlike the common observations in mainstream additive manufacturing of metallic materials, which eliminates pores and achieves almost fully dense material for attaining high-performance components, this work emphasizes the positive roles of limited engineering pores in inhibiting cracks and improving the manufacturability of LDED-processed high-strength Al alloy. The superior strength-ductility synergy achieved in 7075 Al alloy could be attributed to the positive effects of engineered porosities (around 1.14%) in materials. Further increasing energy input significantly reduced porosity to about 0.5% at the expense of inducing cracking. The pores were found to break the epitaxial growth of columnar grains, promote the formation of low-angle grain boundaries and near-equiaxed grains and sustain higher stress levels, which effectively reduced stress in the rest parts and suppressed the cracking. The LDED-processed 7075 Al alloy, featuring tailored internal pores, achieved a yield strength of 356 MPa, tensile strength of 464 MPa, and elongation of 9.7%, showing superior strength-ductility synergy compared to the LDED, LPBF and cast processed 7075 Al alloys reported in the literature. The presence of fine precipitates (averaging 3.2 nm) and high-density dislocations primarily contributed to the alloy's strengthening. Additionally, the pores in the 7075 Al alloy contribute to ductility enhancement by dispersing stress through multipoint stress intensification, thus delaying stress concentration at specific sites. It's worth acknowledging the study's limitation, as the small size of the LDED-processed Al block ($80\times50\times8$ mm^3) may not guarantee crack-free when scaling up to large components. Nevertheless, this work offers valuable insights into the interplay between pores and cracks for achieving high performance and manufacturability in additive manufacturing of high cracking-susceptibility alloys.

Disclosure statement

No potential conflict of interest was reported by the authors.

References

[1] T.-S. Liu, F. Qiu, H.-Y. Yang, S. Liu, Q.-C. Jiang, L.-C. Zhang, Exploring the potential of FSW-ed Al–Zn–Mg–Cu-based composite reinforced by trace in-situ nanoparticles in manufacturing workpiece with customizable size and high mechanical performances, Compos. Part B: Eng. 250 (2023) 110425. 10.1016/j.compositesb.2022.110425

[2] S. Zhang, Y. Li, A. Frederick, Y. Wang, Y. Wang, L. Allard, M. Koehler, S. Shin, A. Hu, Z. Feng, In-situ formation of Al3Ni nano particles in synthesis of Al 7075 alloy by friction stir processing with Ni powder addition, J. Mater. Process. Tech. 311 (2023) 117803. 10.1016/j.jmatprotec.2022.117803

[3] A. Wang, Q. Wei, Z. Tang, P. Ren, X. Zhang, Y. Wu, H. Wang, A. Du Plessis, J. Huang, K. Hu, H. Wang, Effects of processing parameters on pore defects in blue laser directed energy deposition of aluminum by in and ex situ observation, J. Mater. Process. Tech. 319 (2023) 118068. 10.1016/j.jmatprotec.2023.118068

[4] Y. Zeng, J. Guo, J. Zhang, W. Yang, L. Li, The Microstructure characteristic and Its influence on the stray grains of Nickel-based single crystal superalloys prepared by Laser directed energy deposition, J. Mater. Process. Tech. 329 (2024) 118443. 10.1016/j.jmatprotec.2024.118443

[5] J.H. Martin, B.D. Yahata, J.M. Hundley, J.A. Mayer, T.A. Schaedler, T.M. Pollock, 3D printing of high-strength aluminium alloys, Nature 549 (2017) 365-369. 10.1038/nature23894

[6] D. Svetlizky, M. Das, B. Zheng, A.L. Vyatskikh, S. Bose, A. Bandyopadhyay, J.M. Schoenung, E.J. Lavernia, N. Eliaz, Directed energy deposition (DED) additive manufacturing: Physical characteristics, defects, challenges and applications, Mater. Today 49 (2021) 271-295. 10.1016/j.mattod.2021.03.020

[7] A. Singh, A. Ramakrishnan, D. Baker, A. Biswas, G.P. Dinda, Laser metal deposition of nickel coated Al 7050 alloy, J. Alloys Compd. 719 (2017) 151-158. 10.1016/j.jallcom.2017.05.171

[8] T.C. Lin, C. Cao, M. Sokoluk, L. Jiang, X. Wang, J.M. Schoenung, E.J. Lavernia, X. Li, Aluminum with dispersed nanoparticles by laser additive manufacturing, Nat. Commun. 10 (2019) 4124. 10.1038/s41467-019-12047-2

[9] D. Svetlizky, B. Zheng, T. Buta, Y. Zhou, O. Golan, U. Breiman, R. Haj-Ali, J.M. Schoenung, E.J. Lavernia, N. Eliaz, Directed energy deposition of Al 5xxx alloy using Laser Engineered Net Shaping (LENS®), Mater. Design 192 (2020) 108763. 10.1016/j.matdes.2020.108763

[10] M. Ansari, E. Jabari, E. Toyserkani, Opportunities and challenges in additive manufacturing of functionally graded metallic materials via powder-fed laser directed energy deposition: A review, J. Mater. Process. Tech. 294 (2021) 117117. 10.1016/j.jmatprotec.2021.117117

[11] Y. Zhang, L. Wu, X. Guo, S. Kane, Y. Deng, Y.-G. Jung, J.-H. Lee, J. Zhang, Additive Manufacturing of Metallic Materials: A Review, J. Mater. Eng. Perform. 27 (2017) 1-13. 10.1007/s11665-017-2747-y

[12] D. Svetlizky, B. Zheng, A. Vyatskikh, M. Das, S. Bose, A. Bandyopadhyay, J.M. Schoenung, E.J. Lavernia, N. Eliaz, Laser-based directed energy deposition (DED-LB) of advanced materials, Mater. Sci. Eng.: A 840 (2022) 142967. 10.1016/j.msea.2022.142967

[13] T.-S. Liu, P. Chen, F. Qiu, H.-Y. Yang, N.T.Y. Jin, Y. Chew, D. Wang, R. Li, Q.-C. Jiang, C. Tan, Review on laser directed energy deposited aluminum alloys, Int. J. Extrem. Manuf. 6 (2024) 022004. 10.1088/2631-7990/ad16bb

[14] H. Yang, J. Sha, D. Zhao, F. He, Z. Ma, C. He, C. Shi, N. Zhao, Defects control of aluminum alloys and their composites fabricated via laser powder bed fusion: A review, J. Mater. Process. Tech. 319 (2023) 118064. 10.1016/j.jmatprotec.2023.118064

[15] H. Wang, B. Gould, M. Moorehead, M. Haddad, A. Couet, S.J. Wolff, In situ X-ray and thermal imaging of refractory high entropy alloying during laser directed deposition, J. Mater. Process. Tech. 299 (2022) 117363. 10.1016/j.jmatprotec.2021.117363

[16] Z. Tao, A. Thanki, L. Goossens, A. Witvrouw, B. Vrancken, W. Dewulf, Photodiode-based porosity prediction in laser powder bed fusion considering inter-hatch and inter-layer effects, J. Mater. Process. Tech. 332 (2024) 118539. 10.1016/j.jmatprotec.2024.118539

[17] G. Li, X. Li, C. Guo, Y. Zhou, Q. Tan, W. Qu, X. Li, X. Hu, M.-X. Zhang, Q. Zhu, Investigation into the effect of energy density on densification, surface roughness and loss of alloying elements of 7075 aluminium alloy processed by laser powder bed fusion, Opt. Laser Technol. 147 (2022) 107621. 10.1016/j.optlastec.2021.107621

[18] W. Li, F. Qian, J. Li, Y. Zhu, Y. Liang, S. Xu, Y. Li, X. Cheng, Design strategy for eliminating cracking and improving mechanical properties of Al-Mg-Si alloys fabricated by laser melting deposition, Addit. Manuf. 68 (2023) 103513. 10.1016/j.addma.2023.103513

[19] Y. Liu, F. Wang, D. Xu, J. Wang, F. Jiang, M. Zarinejad, Y. Tong, Microstructure and mechanical properties of laser metal deposited Ti6Al4V alloy with near equiaxed β grain structure, J. Mater. Res. Technol. 22 (2023) 1935-1947. 10.1016/j.jmrt.2022.12.068

[20] T.-S. Liu, F. Qiu, H.-Y. Yang, C.-L. Tan, B.-X. Dong, J.-F. Xie, S.-L. Shu, Q.-C. Jiang, L.-C. Zhang, Versatility of trace nano-TiC–TiB2 in collaborative control of solidification-rolling-welding microstructural evolution in Al–Mg–Si alloy for enhanced properties, Mater. Sci. Eng.: A 851 (2022). 10.1016/j.msea.2022.143661

[21] G. Li, C. Zhao, Y. Huang, Q. Tan, J. Hou, X. He, C. Guo, W. Lu, L. Zhou, S. Liu, L. Zhang, X. Chen, X. Li, Y. Li, J. Luan, Z. Li, X. Mao, M.-X. Zhang, Q. Zhu, J. Lu, Additively manufactured fine-grained ultrahigh-strength bulk aluminum alloys with nanostructured strengthening defects, Mater. Today 76 (2024) 40-51. 10.1016/j.mattod.2024.05.006

[22] R. Li, M. Wang, Z. Li, P. Cao, T. Yuan, H. Zhu, Developing a high-strength Al-Mg-Si-Sc-Zr alloy for selective laser melting: Crack-inhibiting and multiple strengthening mechanisms, Acta Mater. 193 (2020) 83-98. 10.1016/j.actamat.2020.03.060

[23] F. Liu, Z.Y. Liu, G.Y. He, L.N. Ou, Dislocation ordering and texture strengthening of naturally aged Al-Cu-Mg alloy, J. Mater. Sci. Technol. 118 (2022) 1-14. 10.1016/j.jmst.2021.12.011

[24] C. Tan, Y. Chew, F. Weng, S. Sui, Z. Du, F.L. Ng, G. Bi, Superior strength-ductility in laser aided additive manufactured high-strength steel by combination of intrinsic tempering and heat treatment, Virtual Phys. Prototy. 16 (2021) 460-480. 10.1080/17452759.2021.1964268

[25] Y. Weng, L. Ding, Z. Zhang, Z. Jia, B. Wen, Y. Liu, S. Muraishi, Y. Li, Q. Liu, Effect of Ag addition on the precipitation evolution and interfacial segregation for Al–Mg–Si alloy, Acta Mater. 180 (2019) 301-316. 10.1016/j.actamat.2019.09.015

[26] J. Chen, Y. Zhao, D. Song, Z. Wang, Z. Luo, W. Zhang, Effects of applied pressure and residual heat quenching on the mechanical and thermal properties of cast Al–Mg–Zn–Mn–Fe alloys, Mater. Sci. Eng.: A 892 (2024) 146030. 10.1016/j.msea.2023.146030

[27] Y.-T. Mo, C. Wang, S.-Y. Zhang, X. Liu, M. Zha, J.-H. Luan, Z.-B. Jiao, H.-Y. Wang, Achieving high strength-ductility synergy through high-density coherent precipitation in twin-roll cast Al–Zn–Mg–Cu strips, Mater. Sci. Eng.: A 850 (2022) 143592. 10.1016/j.msea.2022.143592

[28] D. Liu, D. Wu, C. Ge, H. Lu, Z. Chen, M. Liu, Y. Wang, F. Niu, G. Ma, K. Luo, J. Lu, Superior strength of laser-arc hybrid additive manufactured Al-Zn-Mg-Cu alloy enabled by a tunable microstructure, Addit. Manuf. 68 (2023) 103526. 10.1016/j.addma.2023.103526

[29] K. Ma, H. Wen, T. Hu, T.D. Topping, D. Isheim, D.N. Seidman, E.J. Lavernia, J.M. Schoenung, Mechanical behavior and strengthening mechanisms in ultrafine grain precipitation-strengthened aluminum alloy, Acta Mater. 62 (2014) 141-155. 10.1016/j.actamat.2013.09.042